PHYSICAL REVIEW E **67**, 066308 (2003)

Thermocapillary-buoyancy convection in a shallow cavity heated from the side

V. M. Shevtsova,[1] A. A. Nepomnyashchy,[2,*] and J. C. Legros[1,†]
[1]*Université Libre de Bruxelles, MRC, CP-165/62, 50, av. F. D. Roosevelt, B-1050 Brussels, Belgium*
[2]*Department of Mathematics and Minerva Center for Nonlinear Physics of Complex Systems,*
Technion-Israel Institute of Technology, Haifa, Israel
(Received 21 October 2002; published 27 June 2003)

Combined thermocapillary-buoyancy convection has been investigated numerically in an extended cavity with differently heated walls. When the Marangoni number Ma grows, the unicellular flow is replaced by a steady bicellular or multicellular flow and then either by a hydrothermal wave or an oscillatory multicellular flow, depending on the dynamic Bond number Bo_{dyn}. The appearance of a hydrothermal wave prevents the propagation of the stationary roll structure, which spreads from the hot side, over the whole cavity. The hydrothermal wave itself looks as a succession of the cells *moving* from the cold side towards the motionless rolls on the hot side. For an intermediate interval of Bo_{dyn} the parallel flow is unstable with respect to the hydrothermal wave (HTW), but the multicellular periodic structure generated by the side-wall perturbation is stable, so that the HTW decays in space when propagating on the background of the multicellular structure. The nonlinear competition between finite-amplitude, boundary-induced steady patterns and hydrothermal waves is essential. A nonlinear simulation of flow regimes in a wide region of the values of dynamical Bond number and Marangoni number is presented. A number of phenomena that cannot be predicted in the framework of the linear stability theory, specifically those characteristic for the motion in the intermediate interval of Bo_{dyn}, as well as the secondary transition from steady to unsteady flows at large Bo_{dyn}, which takes place when the Marangoni number Ma grows, are described.

DOI: 10.1103/PhysRevE.67.066308 PACS number(s): 47.27.−i, 44.27.+g, 44.25.+f

I. INTRODUCTION

During the past decades, convective flows in systems with free boundaries attracted much attention, specifically due to their relevance to crystal growth processes under microgravity conditions [1]. The simplest convective flow appears when a free surface of an extended liquid layer is subject to a horizontal temperature gradient [2]. This nearly parallel convective flow is produced by a combined action of two effects, the buoyancy and the thermocapillary effect. The relative weight of each effect is determined by the so called dynamic Bond number Bo_{dyn} which is the ratio of the Rayleigh number Ra and the Marangoni number Ma. The parallel convective flow becomes unstable when the temperature gradient increases.

The first experiments on the wave instability have been done by Volkoviski [3] (1935), who investigated the propagation of a thermocapillary flow from warm container onto the inclined plate. In the case of a purely thermocapillary flow ($\mathrm{Bo}_{dyn}=0$), several instability modes have been found by Smith and Davis [4–7]. The most widespread type of instability, *hydrothermal* instability, leads to the appearance of oblique waves moving upstream [4]. The numerical simulations justify the predictions of the linear stability analysis [8].

Under the combined action of thermocapillarity and buoyancy ($\mathrm{Bo}_{dyn}\neq 0$), a transition from oblique, three-dimensional, hydrothermal waves to two-dimensional waves moving downstream has been predicted by the linear stability theory [9] and observed experimentally [10] (see also Ref. [11]). Surprisingly, many experiments [12–15] revealed the appearance of one more flow pattern, *steady* transverse multicellular pattern (''cat's-eyes flow''), in an apparent disagreement with the theory. The explanation of this paradox was given by Priede and Gerbeth [16]. The standard linear stability theory determines the threshold of a *convective* instability, i.e., the instability which develops in the reference frame *moving* with the group velocity of waves [17]. The local growth of disturbances, which leads to an experimentally observable wavy motion, starts after crossing another boundary in the parameter space which is called the *absolute* instability boundary. In the region of convective instability, the crucial point is the influence of rigid lateral walls which produces steady vortexlike disturbances of the flow. These finite-amplitude boundary disturbances generate a steady structure which either decays in space and therefore is localized near the lateral boundary (in the case of the ''nontransparency'') or fills the whole layer forming a steady multicellular pattern (in the case of the ''amplification'') [17]. According to the extended linear stability theory developed by Priede and Gerbeth [16] (the calculations have been done for $\mathrm{Pr}=13.9$), for relatively small values of the dynamical Bond number, $\mathrm{Bo}_{dyn}<0.2$, the boundary of the absolute instability is rather close to that of the convective instability, that is why the standard linear stability theory gives a rather good prediction. In an intermediate interval, $0.2<Bo_{dyn}<0.3$, the boundary of the absolute instability is still lower than that of the development of a steady multicellular flow in the whole layer, but it is much higher than the boundary of the convective instability. For larger values of Bo_{dyn}, $\mathrm{Bo}_{dyn}>0.3$, the parallel flow is replaced by the steady mul-

---

*Electronic address: nepom@math.technion.ac.il
†Electronic address: vshev@ulb.ac.be http://www.ulb.ac.be/polytech/mrc

1063-651X/2003/67(6)/066308(14)/$20.00

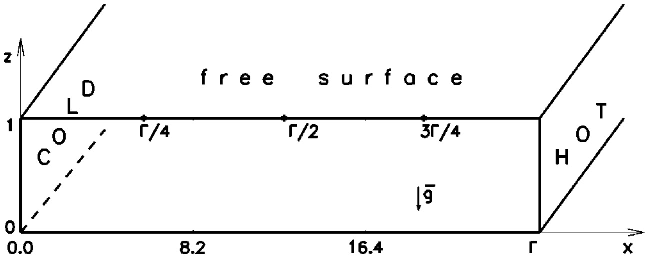

FIG. 1. Geometry of the system. The aspect ratio is $\Gamma=24.7$.

ticellular flow produced by the lateral boundary. The predictions of the extended linear stability theory agree well with experimental observations [14,15]. Note that the appearance of boundary-induced steady patterns on the background of an oscillatory-unstable steady state is known also for chemical reaction-diffusion systems [18–20].

However, the linear theory is unable to predict the motion in the intermediate interval of Bo_{dyn}, where the nonlinear competition between finite-amplitude, boundary-induced steady patterns and hydrothermal waves is essential. It also cannot describe the secondary transition from steady to unsteady flows at large Bo_{dyn}, which takes place when the Marangoni number Ma grows. In order to investigate the above-mentioned phenomena, we have carried out in the present paper a nonlinear simulation of flow regimes in a wide region of values of dynamical Bond number and Marangoni number. In Sec. II, we give a mathematical formulation of the problem and describe the numerical method. In Sec. III, the results of the simulation are presented. A special attention is paid to the essentially nonlinear phenomena. Section IV contains the discussion of results and conclusions.

II. FORMULATION OF THE PROBLEM

Thermocapillary and buoyancy convection are considered in a high-Prandtl fluid filling the rectangular cavity of the depth d and the length L (see Fig. 1). Two vertical isothermal side walls are kept at the temperature T_0 on the left and at the temperature T_h on the right ($\Delta T=T_h-T_0$). Both bottom and top boundaries are assumed to be thermally isolated. The fluid is supposed to be Newtonian and the surface tension σ on the free surface is a linear function of the temperature T, $\sigma=\sigma_0-\gamma(T-T_0)$, where $\gamma=-\partial\sigma/\partial T$ is assumed to be constant and positive. It is assumed that the dependence of the viscosity upon the temperature does not play an important role as the applied temperature difference is rather small [21], therefore we ignore it in our analysis. We consider two-dimensional flows with velocity components (U,W) and define the stream function ψ and the vorticity ω by formulas

$$\omega=\frac{\partial U}{\partial z}-\frac{\partial W}{\partial x},\quad U=\frac{\partial\psi}{\partial z},\quad W=-\frac{\partial\psi}{\partial x}.$$

We scale the problem by using d, d^2/ν, ν/d, ν/d^2, ν as units for the length, time, velocity, vorticity, and the stream function, where ν is the kinematic viscosity. The dimensionless temperature is defined as $\Theta_0=(T-T_0)/\Delta T$. It is convenient to define also the deviation from the linear temperature profile $\Theta=\Theta_0-x/\Gamma$, where $\Gamma=L/d$ is the aspect ratio.

In variables ψ,ω the governing equations in Boussinesq approximation are written as

$$\frac{\partial\omega}{\partial t}+U\frac{\partial\omega}{\partial x}+W\frac{\partial\omega}{\partial z}=\nabla^2\omega-Gr_m\left(\frac{\partial\Theta}{\partial x}+\Gamma^{-1}\right),\tag{1}$$

$$\frac{\partial\Theta}{\partial t}+U\Gamma^{-1}+U\frac{\partial\Theta}{\partial x}+W\frac{\partial\Theta}{\partial z}=\frac{1}{\mathrm{Pr}}\nabla^2\Theta,\tag{2}$$

$$\nabla^2\psi=\omega,\quad 0\leqslant x\leqslant\Gamma,\quad 0\leqslant z\leqslant 1,\tag{3}$$

where

$$\nabla^2=\partial^2_{xx}+\partial^2_{zz},$$

with boundary conditions at rigid surfaces $x=0$, $x=\Gamma$:

$$\Theta=0,\quad \psi=0,\quad \partial\psi/\partial x=0,\tag{4}$$

at the bottom $z=0$,

$$\partial_z\Theta=0,\quad \psi=0,\quad \partial\psi/\partial z=0,\tag{5}$$

at the free surface $z=1$,

$$\partial_z\Theta=0,\quad \psi=0,\quad \omega=-\mathrm{Re}_m\left(\frac{\partial\Theta}{\partial x}+\Gamma^{-1}\right).\tag{6}$$

The dimensionless parameters which appear in Eqs. (1)–(6) are the thermocapillary Reynolds number, Grashof number, and Prandtl number: $\mathrm{Re}_m=\gamma\Delta T d/\rho\nu^2$, $\mathrm{Gr}_m=g\beta\Delta T d^3/\nu^2$, $\mathrm{Pr}=\nu/k$, where ρ is the density of the liquid, g is the gravity acceleration, β is the heat expansion coefficient, and k is the thermal diffusion coefficient. Index m means "mathematical" (see below). One can define also the Marangoni number $\mathrm{Ma}_m=\mathrm{Re}_m\mathrm{Pr}$ and the Rayleigh number $\mathrm{Ra}_m=\mathrm{Gr}_m\mathrm{Pr}$.

This formal mathematical choice of parameters, though convenient for carrying out the simulations, does not reflect the physical aspects of the problem. Indeed, the characteristic velocity of the flow generated by the thermocapillary stress is proportional to the horizontal component of the temperature gradient, $\Delta T/L$, rather than $\Delta T/d$. Therefore, the physical phenomena are characterized by the modified Reynolds and Grashof numbers [14],

$$\mathrm{Re}=\frac{\gamma d^2}{\rho\nu^2}\frac{\Delta T}{L}=\mathrm{Re}_m/\Gamma,\tag{7}$$

$$\mathrm{Gr}=\frac{g\beta d^4}{\nu^2}\frac{\Delta T}{L}=\mathrm{Gr}_m/\Gamma,\tag{8}$$

as well as by the modified Marangoni and Rayleigh numbers, Ma = Re Pr and Ra = Gr Pr.

It should be taken into account that under the conditions of a real experiment, the geometric parameters of the system, d and L, are not changed while the temperature difference ΔT is varied. Thus, Re and Gr are not independent but proportional, while their ratio, the dynamic Bond number $\mathrm{Bo}_{dyn}=\mathrm{Gr}/\mathrm{Re}=g\rho\beta d^2/\gamma$, is fixed.

Throughout the present study the aspect ratio will remain constant, $\Gamma=24.7$. This choice corresponds to the conditions of the experiment [13] done with $L=74$ mm, $d=3$ mm. Actually, the calculations have been done for two different liquids with close Prandtl numbers: the decane with $\mathrm{Pr}=14.79$ and the 1cSt silicone oil with $\mathrm{Pr}=13.9$ respectively. One may find their physical properties in Refs. [13,14] correspondingly. Most of the results have been obtained for $\mathrm{Pr}=13.9$; the results for $\mathrm{Pr}=14.79$ will be given only for the high Bond numbers, $\mathrm{Bo}_{dyn}\geqslant 0.65$.

For the chosen liquid and aspect ratio, the problem is controlled by two parameters, the dynamic Bond number Bo_{dyn} and the Marangoni number Ma. Note that for the fixed value of Γ, the variation of Bond number means a simultaneous change of the depth of the liquid and the length of the cavity. Because the physical parameters of the fluid are fixed and the depth of the liquid is determined by Bo_{dyn}, we shall describe our results using the dimensional temperature difference ΔT in addition to Ma, so that they can be more easily compared with the experimental data; $Ma=C\,\mathrm{Pr}\,\Gamma^{-1}\sqrt{\mathrm{Bo}_{dyn}}\,\Delta T$. The coefficient $C=(\gamma^3/\rho^3\nu^4\beta g)^{1/2}$ depends only on the physical properties of the liquid. In the case of 1cSt silicone oil, $C=293.89$, where ΔT is measured in degrees Kelvin.

III. NUMERICAL METHOD AND CODE VALIDATION

Although the above written two-dimensional (2D) equations look simple, to carry out the simulations for such a large aspect ratio is not an easy task. To solve the problem, the time-dependent equations are approximated by central differences on a stretched mesh. The smallest step sizes are chosen near the rigid walls and free surface. An alternating direction implicit (ADI) method is used to solve the time-dependent problem for the vorticity, the temperature, and the stream function. The time derivatives are forward differenced. The Poisson equation (3) for ψ is solved by introducing an artificial iterative term, analogous to the time-derivative one. For the convergence of iterations for rather high values of Re_m, the choice of the iteration parameter δ plays a crucial role. Two different approaches are used: (a) for a new set of parameters a constant value of δ was chosen according to Ref. [22]; (b) at the first iteration the value of δ is chosen as $\delta_0=\min(\Delta x_i,\Delta z_j)$ and then δ is strongly increased ($\delta\gg\delta_0$) and slowly moves back further to the initial value δ_0.

Depending upon the characteristic set of parameters, the first or the second approach was used. The numerical steady state solution, if it exists, is obtained by the convergence of the transient calculations.

As a first check of the basic state calculations, the absolute value of the stream function minimum and the Nusselt numbers on the hot and cold walls are compared with those obtained in Ref. [23] (see Table I). The agreement is very good, all the deviations are about 1%.

TABLE I. Comparison of results for $\mathrm{Pr}=1$.

Present work: (61×81)	$\mathrm{Re}\times 10^3$	Nu_{hot}	Nu_{cold}	$\psi_{max}\times 10^{-2}$
Ref. [23]	1	1.93	1.92	0.479
Present result: (ψ/Re)		1.94	1.90	0.483
Ref. [23]	5	3.42	3.41	0.366
Present result: (ψ/Re)		3.45	3.37	0.367

An additional check is made by comparing present results with those given by Ohnishi et al. [24] for $\mathrm{Re}_m=26\,666.7$, $\Gamma=4$, and $\mathrm{Pr}=0.015$. The difference in the values of the stream function maxima obtained for this very high Reynolds number is about 1%: For example, present calculations give $\psi_{max}=107.3$ versus $\psi_{max}=108.6$ in Ref. [24]. For the pure buoyancy convection, the code was also checked using the De Vahl Davis test [25], the results of which are shown in Table II.

All these tests provide a sufficient validation for the present numerical code. The results of grid refinement study are shown in Table III, when $\mathrm{Re}_m=26\,666.7$, $\Gamma=4$, and $\mathrm{Pr}=0.015$.

A nonuniform mesh 301×51 has been used for the basic calculations. For the high values of Reynolds number, $\mathrm{Re}>40$, ($\mathrm{Re}_m>1000$), the calculations were done on the stretched grid 601×101.

IV. DESCRIPTION OF RESULTS

A. Stationary flows

A return flow appears in the liquid layer as soon as the horizontal temperature gradient is established between the lateral walls of the cavity. On the free surface, the liquid is moving from the hot wall towards the cold one due to the Marangoni and buoyancy forces. At very small temperature difference (ΔT) between distant walls, two small cat's-eye vortices appear near the rigid walls. With increasing ΔT these two cat's eyes quickly merge, leading to a single convective cell and then to the appearance of a stronger cell near the hot wall and a larger but weaker cell in the volume. The typical pattern flow of the steady state for the chosen, rather high-Prandtl number fluid, $\mathrm{Pr}=13.9$, is shown in Fig. 2. The levels of 12 isotherms are taken as $\Theta_{0,i}=0.08i$. The streamlines are also chosen equidistant according to the minimal and maximal values of Ψ in the cavity.

TABLE II. Test of De Vahl Davis for buoyancy convection.

	$\mathrm{Ra}=10^3$	$\mathrm{Ra}=10^4$	$\mathrm{Ra}=10^5$	$\mathrm{Ra}=10^6$
Present work	1.654	7.136	13.50	23.57
Ohnishi *et al.* [24]	1.657	7.146	13.59	23.92
De Vahl Davis Bench mark solution [25]	1.653	7.142	13.54	23.59

TABLE III. Convergence on the grid.

Grid	ψ_{max}
100×25	101.57
128×32	104.40
160×40	106.49
200×50	107.33

For a fixed ΔT, the temperature drops grow slowly with the increase of the Bond number, see Fig. 3. For a fixed Bond number, the temperature drops grow faster than the imposed temperature difference between remote walls. As a result, in relatively thick layers, e.g., Bo$=0.728$, just before the onset of oscillatory instability the effective temperature gradient in the core of the cavity $(\partial T/\partial x)$ is up to three times smaller than the imposed $\Delta T/L$, see Ref. [26]. Therefore the effective temperature gradient should be used for the calculations of the critical Marangoni number.

Although the aspect ratio is very large, $\Gamma=24.7$, one can expect that the horizontal temperature gradient in the middle of the cavity will differ from that in an infinite layer, because of the existence of the thermal boundary layer near the rigid vertical walls. It was shown experimentally [14,15] and numerically [26] that the temperature drops exist near both the rigid walls. Despite the fact that the thickness of the thermal boundary layer near the cold wall is much smaller than that near the hot one, the temperature drop is larger near the cold wall.

B. Stability diagram

According to our simulations, further development of the flow structure with the increase of ΔT depends upon the dynamic Bond number: for $\mathrm{Bo}_{dyn}\leqslant 0.25$ the steady flow becomes unstable to hydrothermal waves (HTWs) and for $\mathrm{Bo}_{dyn}\geqslant 0.323$ the steady unicellular state is transformed into a steady multicellular state and then bifurcates to a time-dependent one. The experimental results, reported in Ref. [14], determine a different value of the critical Bond number, $\mathrm{Bo}_{dyn}\approx 0.222$. This discrepancy may have several reasons: (i) it is rather difficult to obtain experimentally that exact values of the critical parameters; (ii) the experiments have been carried out for different values of the aspect ratio; (iii) the numerical results have been obtained in the 2D case with a constant aspect ratio. Although the 2D results correctly reflect the physics of the phenomena, the critical numbers could be slightly different. Note, that the critical Bo_{dyn} observed in our calculations is rather close to the theoretical prediction of Priede and Gerbeth [16].

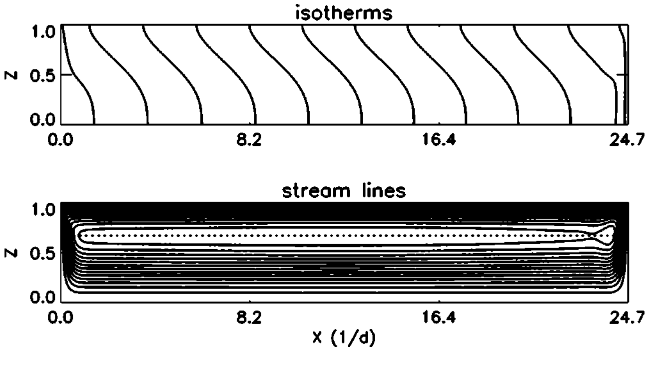

FIG. 2. The steady state distribution of the isotherms of Θ_0 and the isolines of ψ when Pr$=13.9$, $\mathrm{Bo}_{dyn}=0.08$, Ma$=141$ ($\Delta T=3$ K).

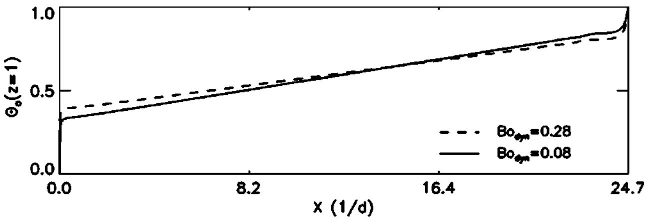

FIG. 3. The temperature distribution along the free surface close to the threshold of the instability: $\mathrm{Bo}_{dyn}=0.08$ when Ma$=607(\Delta T\approx 13$ K) and $\mathrm{Bo}_{dyn}=0.28$ when Ma$=960(\Delta T\approx 11$ K). The large temperature drops exist near the rigid walls.

We have never observed a genuine unicellular flow at the threshold of the appearance of HTWs, but it does exist far below that threshold. The cat's-eyes flow, observed for Ma $\leqslant 100$, is replaced by the one-cell flow, which is detected in a rather narrow region of Marangoni numbers, Ma$\approx(120\pm 20)\%$. For higher Ma, even for the smallest values of the dynamical Bond number Bo_{dyn}, we observed a bicellular flow that consisted of a strong cell near the hot wall and a weaker cell in the rest of the cavity, see Fig. 2. The fluid moves counterclockwise in both cells. The cell near the hot wall has a relatively small size, e.g., in Fig. 2 the ratio of the sizes of these cells in the horizontal direction is 1:21. The maxima of the stream functions are located at the depth $z=2/3$, and the separation of the cells does not go up to the free surface. That could explain why the unicell flow has been observed rather often in the experiments, when the measurements are done near the free surface. For larger values of Bo_{dyn}, several cells developed near the hot wall (see below). Thus, we find that the term "unicellular flow" is not sufficiently accurate for the description of the flow prior to the onset of HTWs, and we shall not use this term hereafter.

The results to be presented here will be focused on the study of the different types of instabilities, arising under the variation of the two control parameters: Bo_{dyn} and Ma. The transition map from steady state (bicellular or multicellular flow) to oscillatory one is shown in Fig. 4 in terms of the critical Marangoni number versus the dynamic Bond number. The value of Ma, at which the oscillations of $\Theta(t)$ or $\psi(t)$ are sustained, is referred to as the critical Marangoni number, Ma$=\mathrm{Ma}_{cr}$. The solid line corresponds to the numerical results; the crosses on the curve indicate the points for which calculations have been done. The diamond at $\mathrm{Bo}_{dyn}=0.18$ when Ma$=741$ corresponds to the experimental point [15] in Fig.2 when $L_x=30$ mm, $h=1.2$ mm, $\Delta T=6$ K. The broken line corresponds to the Marangoni numbers, recalculated through the efficient temperature gradient $(\partial\Theta_0/\partial x)_{mdl}$ in the middle of the cavity:

$$\mathrm{Ma}_{ef}=\mathrm{Ma}\left(\frac{\partial\Theta_0}{\partial x}\right)_{mdl}\left(\frac{\Delta T}{L}\right)^{-1}. \tag{9}$$

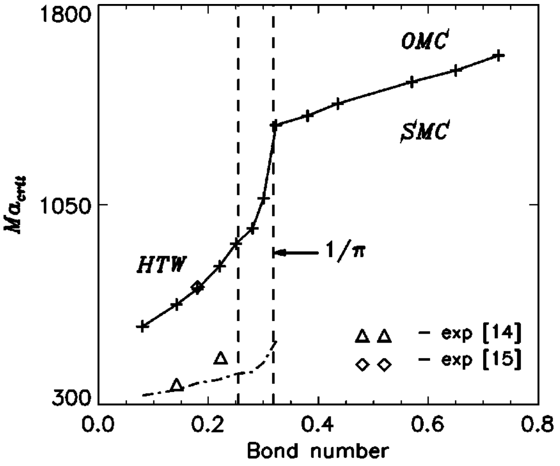

FIG. 4. Stability diagram for $\mathrm{Pr}=13.9$ and $\Gamma=24.7$. The solid line shows the numerical results and the broken line represents some of them, recalculated through the efficient temperature gradient, Eq. (9). The dashed lines confine the transient region between the hydrothermal wave (HTW) and oscillatory multicellular cells (OMC). The steady multicellular cells (SMC) extend up to the HTW, when $\mathrm{Bo}_{dyn}<0.25$.

Actually, for the oscillatory multicellular flow (see below), it is rather difficult to determine precisely the effective temperature gradient, as the temperature distribution along the cavity has a pronounced wavy profile. Triangles on the broken line show the experimental results of Riley and Neitzel [14] in terms of Ma_{ef}. For the Bond numbers $\mathrm{Bo}<0.222$, when the hydrothermal waves were observed in the experiment, the results are in a good agreement.

Note that the effective critical Marangoni Ma_{ef} in the limit $\mathrm{Bo}_{dyn}\rightarrow 0$ also well agrees well with the theoretical prediction of Smith and Davis [4]. The broken line can be continued with the same slope as

$$\mathrm{Ma}_{ef}^{cr}=290+474.82\mathrm{Bo}_{dyn},$$

and it gives $\mathrm{Ma}_{ef}^{cr}=290$ for the infinite layer versus $\mathrm{Ma}\approx 267$ for $\mathrm{Pr}=9.25$ in [4].

The stability diagram in Fig. 4 can be roughly separated into three regions, according to the slope of the curve $\mathrm{Ma}(\mathrm{Bo}_{dyn})$. Note that the treatment of our results reveals a curious fact, namely, that the oscillatory multicellular states begin when Bo_{dyn} achieves $1/\pi$. (It corresponds to $\mathrm{Bo}_{dyn}\approx 0.32$.) It may be a sign of a possible analytical solution.

C. Multicellular structures and time-periodic hydrothermal waves at small values of the dynamic Bond number

In the present section, we consider the left part of this curve, $0.0<\mathrm{Bo}_{dyn}\leqslant 0.25$, where the HTW dominates. For the small depth of cavity, $\mathrm{Bo}_{dyn}<0.3$, with the increase of the temperature difference a few rolls (more than one) may appear near the hot wall. The transition from one-roll to multiroll flow structure *is not* a result of instability. It is caused by the influence of the lateral wall that generates a wave, stationary in time, but spatially spreading towards the cold side with the increase of the applied temperature gradient. For such a wave the functions Θ,ψ are approximately proportional to the real part of $\exp(ikx+\phi_{\Theta,\psi})$, and $k=k_r+ik_i$, $k_i<0$. The quantity $1/|k_i|$ characterizes the length of the penetration into the cavity for a perturbation generated by the side wall. If $1/|k_i|>\Gamma$, the multiroll structure is observed over the whole cavity.

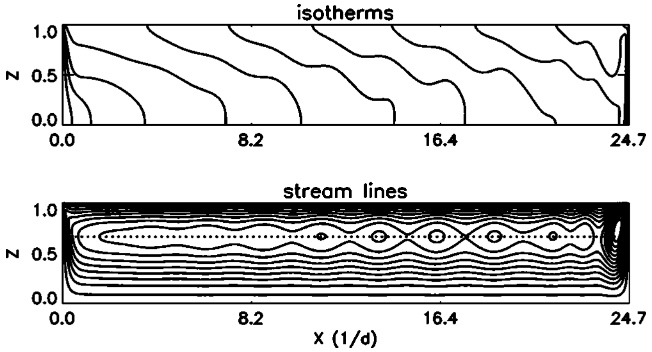

FIG. 5. Snapshot of the isotherms of Θ_0 and isolines of the stream function ψ when $\mathrm{Bo}_{dyn}=0.08$, $\epsilon=0.0465$, $\mathrm{Ma}=636$ [$\Theta_{0,i}=0.08i$, $\psi_i=\psi_{min}+\Delta\psi(0.5+i)$].

The next transition corresponds to the birth of a hydrothermal wave at the cold wall. This hydrothermal wave, moving from the cold side, appears earlier than the rolls coming from the hot side occupying the whole cavity. Eventually, the hydrothermal wave is observed as a succession of the rolls moving from the cold side towards the motionless rolls on the hot side.

A snapshot of the distribution of the isotherms and the streamlines in the cavity is shown in Fig. 5 for the Bond number $\mathrm{Bo}_{dyn}=0.08$ at the temperature difference slightly above the critical value of the onset of the hydrothermal waves: $\mathrm{Ma}=636$ and $\epsilon=(\mathrm{Ma}-\mathrm{Ma}_{cr})/\mathrm{Ma}_{cr}\approx 0.0465$. As soon as the applied temperature difference exceeds a certain value, the hydrothermal wave, generated in the cold part of the cavity, propagates from the left to the right. Recall that the motion of rolls in the direction from the cold end to the hot end is a characteristic feature of the HTWs [4].

One may see in Fig. 5 that the centers of the rolls are located on the line $z\approx 2/3$, and with the increase of the Bond number they retain their position in the vertical direction along this line. In the horizontal direction, the rolls perform a translational motion towards the hot end above the onset of instability. Only far away from the threshold of the instability, $\epsilon>1$, do they start to move in the vertical direction. Therefore it is useful to observe the temporal behavior of the stream function along this line, $z=2/3$.

To demonstrate that the HTW is moving from the cold side towards the hot side, the distributions of the stream function along the cavity on the height $z=2/3$ are shown in Fig. 6(a) during half the period of the oscillation near the threshold of instability. The solid line corresponds to the instant $t=t_0$ and the other curves are given with a time interval $\Delta t=\Pi/10$, where Π is the full period. It is obvious that the HTW is propagating from the cold side towards the hot one. Note that the strength of the steady roll near the hot wall (the maximal value of ψ in the vortex center) is much larger than that of the other ones. To display better the characteristics of

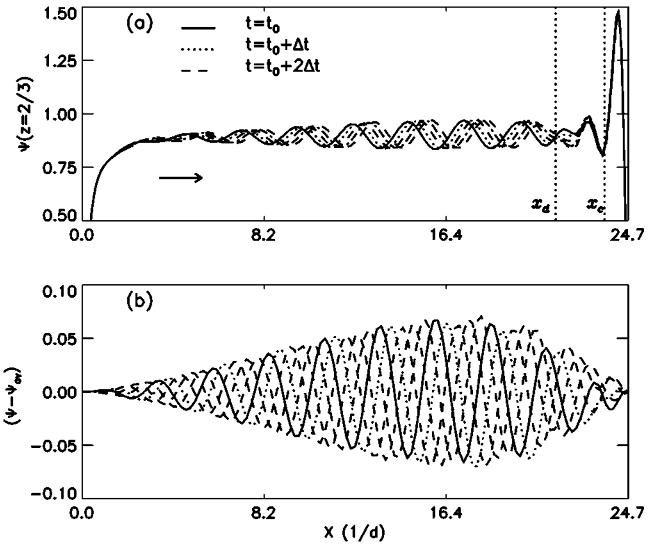

FIG. 6. Instant values of (a) $\psi(t_i)$ over the half period and (b) deviation from average $\tilde{\psi}(t_i)=\psi(t_i)-\psi_{av}$ when $z=2/3$, $\mathrm{Bo}_{dyn}=0.08$, $\mathrm{Ma}=600.4\approx\mathrm{Ma}_{cr}$ ($\Delta T=12.8$).

the HTW propagation, the deviation of the stream function from the average value over the whole period of the oscillations, $\tilde{\psi}(t)=\psi(t)-\psi_{av}$, is shown in Fig. 6(b) along the cavity at the same depth $z=2/3$. The different curves are presented with the time step $\Delta t=\Pi/5$. As it follows from Fig. 6(b), the amplitude of the oscillations of the HTW is increasing with receding from the cold wall.

For this set of parameters, the HTW collides with the only one steady roll (see also Fig. 5), the left boundary of which is rather close to the hot wall, $x_c\approx 23.9$. The hydrothermal wave ‘‘feels’’ the presence of the steady roll: it decays in the region $21.1<x<23.9$. Here it is defined that the wave starts to decay when not only the amplitude of the oscillations decreases but also the oscillations become nonharmonic and succession of the snapshots in time is out of order. From the right side it is confined by the steady roll. The vertical dotted lines at $x_d=21.1$ and $x_c=23.9$ in Figs. 6(a) and 6(b) frame the area of the decay. The amplitude of oscillations has a pronounced peak, $\tilde{\psi}(t)_{max}=0.071$, and it is achieved rather close to the hot wall, $x\approx 18$. With increasing Marangoni number, the amplitude of the oscillations grows and the maximum of the amplitude slowly shifts to the middle of the cavity. For example, for $\mathrm{Ma}=636, \epsilon=0.0465$ the maximal value of the deviations is $\tilde{\psi}(t_i)=0.1568$ and it is located at $x\approx 15.3$.

The situation in the case, when $\mathrm{Bo}_{dyn}=0.142$ and $\mathrm{Ma}=735$, is shown in Fig. 7. For this set of parameters the amplitude of the oscillations is saturated, and it is almost constant in the central part of the cavity, while the HTW decays significantly near the hot side, in the region $20.6<x<23.4$. Again, one motionless roll is established at the hot side before the HTW starts to propagate from the cold side. As ϵ is higher in this case than in the previous one, shown in Fig. 6, the HTW is relatively stronger.

Particularly for this case, $\mathrm{Bo}_{dyn}=0.142$, $\epsilon=0.083$, the intensity of the HTW is sufficient to produce forced oscillations of the steady roll (see Fig. 7). It oscillates with the frequency characteristic for the HTW, $f=0.519$. The amplitude of the oscillations of the steady roll near the hot wall is not negligible. Note that the maximum and minimum deviations of the stream function $\tilde{\psi}$ within the oscillation period are located at the same x position. It means that this roll oscillates in time but its center is motionless in space.

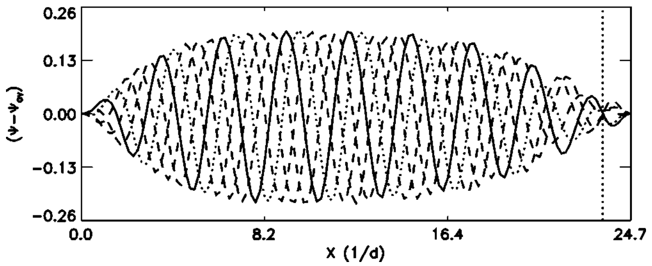

FIG. 7. Five snapshots of the stream function deviation from average $\tilde{\psi}(t_i)=\psi(t_i)-\psi_{av}$ when $z=2/3$, $\mathrm{Bo}_{dyn}=0.142$, $\mathrm{Ma}=735$, $\epsilon=0.083$ ($\Delta T=11.8$).

With increasing Bond number, the critical temperature difference ΔT_{cr}, at which the HTW arises on the cold wall, increases. Recall that with a growth of ΔT, the amount of steady rolls established near the hot side is also increasing. Moreover, the strength of each of them increases faster than that of the waves near the cold side. Therefore the region of the collision of the HTW and steady rolls is slowly shifted away from the hot side towards the cold one, until the Bond number achieves the value $\mathrm{Bo}_{dyn}\approx 0.25$.

For the comparison of the development of two structures, the wavy one and the steady one, related to different sides of the cavity, let us introduce a new characteristic, the ratio of the maximal value of the stream function in the region ‘‘conquered’’ by the steady rolls to the maximal value of ψ in the HTW spreading from the cold side,

$$rs_{\psi}=\max(\psi_{rs})/\max(\psi_{HTW}).$$

Actually, in the multicellular structure the first cell near the hot side always has the maximal value of the stream function, therefore, $\max(\psi_{rs})$ is the maximal ψ inside the first roll.

The dependence of this value rs_{ψ} upon the Bond number is given in Table IV for approximately the same distance from the critical point, ϵ. The growth of rs_{ψ}, with the Bond number, confirms the increasing role of the steady rolls. For this region of Bond numbers, where the HTW dominates, the points can be fitted by a linear law

$$rs_{\psi}=1.3+1.841\mathrm{Bo}_{dyn}.$$

TABLE IV. The dependence of rs_{ψ} upon the Bond number when the HTW dominates.

Bo_{dyn}	0.08	0.142	0.18	0.22	0.25
ϵ	0.0302	0.03125	0.0308	0.034	0.030
rs_{ψ}	1.441	1.560	1.636	1.699	1.754

TABLE V. Evolution of rs_{ψ} when moving above the threshold of instability, $\mathrm{Bo}_{dyn}=0.142$.

Ma	678	699	735	780	881
ϵ	0.002	0.031	0.083	0.15	0.30
rs_{ψ}	1.652	1.560	1.477	1.378	1.278

Further, like in the stability diagram (see Fig. 4), the slope will change.

When moving into the supercritical region while keeping the Bond number constant, one can find that the relative importance of the HTW grows. It is confirmed by the decrease of the parameter rs_{ψ} with the growth of ϵ, shown in Table V for $\mathrm{Bo}_{dyn}=0.142$.

Despite the complicated spatial structure of the flow, the temporal evolution of patterns in the region $\mathrm{Bo}_{dyn}\leqslant 0.25$ is perfectly periodic in time. The analysis of the numerical results reveals that the oscillations produced by the HTW have a rather low frequency, which changes very slowly with increasing of the depth of the liquid layer, e.g., $f=0.52$ for $\mathrm{Bo}_{dyn}=0.08$ and $f=0.48$ for $\mathrm{Bo}_{dyn}=0.30$. It corresponds to the dimensional frequency $f\approx 0.5$ Hz for silicone oil 1cSt and the depth of the layer 1 mm. By the order of magnitude it is in excellent agreement with a frequency, measured in experiments [14]. Another experimental value of the nondimensional frequency, $\omega=9.23$, from Table IV in Ref. [15] obtained in case of $L_x=30$ mm, $h=1.2$ mm, differs from our value, which is equal to $\omega=9.96$ after being recalculated in the variables of Ref. [15] , only by 8%, though the Prandtl numbers in the experiment and in the simulations are different: $\mathrm{Pr}_{ex}=10.3$ versus $\mathrm{Pr}=13.9$.

At $\mathrm{Bo}_{dyn}>0.25$, the oscillations become more complex.

D. Modulated hydrothermal waves in the intermediate interval of Bo_{dyn}

The second range on the stability diagram, $0.25<\mathrm{Bo}_{dyn}\leqslant 0.30$, corresponds to the qualitative change in the development of the flow organization. One of the characteristic features is the change of the slope on the stability diagram, see Fig. 4. The variation of the intensity of the stream function with time along the cavity on the line z=2/3 is shown in Fig. 8 for $\mathrm{Bo}_{dyn}=0.28$. Five steady rolls, which are born on the hot wall, fill the part of the cavity with $x_c=16.7$.

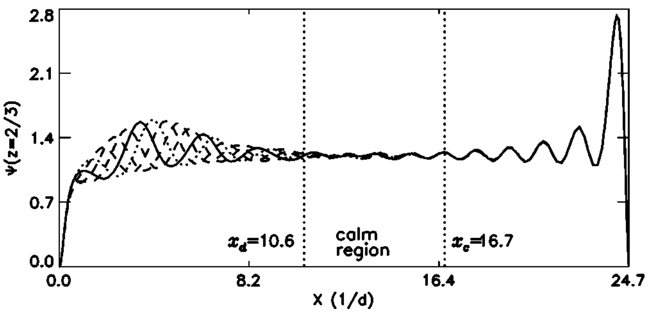

FIG. 8. Distribution of Ψ_i along the cavity over the half period of oscillations at fixed time moments. $\mathrm{Bo}_{dyn}=0.28$, Ma=989, $\epsilon=0.029$.

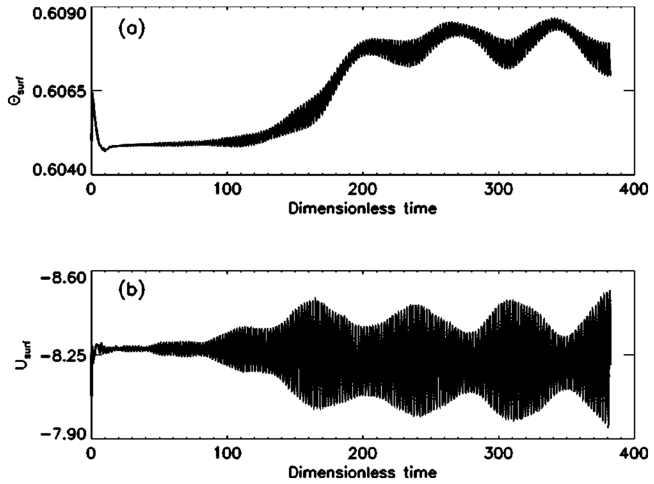

FIG. 9. Dependence of the temperature Θ_0 (a) and the velocity (b) upon time at the middle of the cavity on the free surface, $x=\Gamma/2$ for $\mathrm{Bo}_{dyn}=0.28$, Ma=989, $\epsilon=0.029$.

Figure 8 corresponds to the flow structure slightly above the onset of instability, Ma=989, and $\epsilon=0.029$. The hydrothermal wave, moving from the cold side faces a strong "resistance" of the steady rolls. This means that while the parallel flow is unstable with respect to the HTW, the multicellular periodic structure generated by the side-wall perturbation is stable, so that the HTW decays in space when propagating on the background of the multicellular structure. On one hand, under the impact of the powerful HTW all the rolls that belong to the multicellular structure oscillate in time, but they resist rather strongly and the centers of the rolls do not move in space. Eventually, the amplitude of the temperature oscillations near the hot wall is 32 times smaller than that near the cold side. On the other hand, the HTW loses sharply its power due to the collision with the stationary structure. As a result a calm region (practically vortex-free zone) is observed in the central part of the cavity, $10.6<x<16.7$.

Let us discuss now the temporal evolution of patterns at $\mathrm{Bo}_{dyn}=0.28$. The oscillations of the temperature and the velocity with time in the middle of the cavity, $x=\Gamma/2$, are shown in Fig. 9. Obviously, the observed hydrothermal wave is *modulated in time*. The hydrothermal wave for $\mathrm{Bo}_{dyn}=0.28$ has a fundamental frequency $f_0=0.476$, but also two more close frequencies, $f_1=0.488$ and $f_2=0.464$, appear. The Fourier analysis shows that in the middle of the cavity, the component with the frequency f_1 has the amplitude comparable with that for the f_0. The frequency f_2 reaches the maximal amplitude near the collision area, $15.3<x<18.5$. The modulation of the temperature and velocity time dependences in Fig. 9 is caused by these satellite frequencies. The modulation of $\Theta(t)$ and $V(t)$ is observed at first time for $\mathrm{Bo}_{dyn}=0.25$ and exists for all the Bond numbers in this transient range.

We suppose that the modulation of the hydrothermal wave arises due to its collision with a powerful chain of vigorous rolls, which has its own characteristic frequency of oscillations. For the smaller Bo_{dyn} the critical temperature differ-

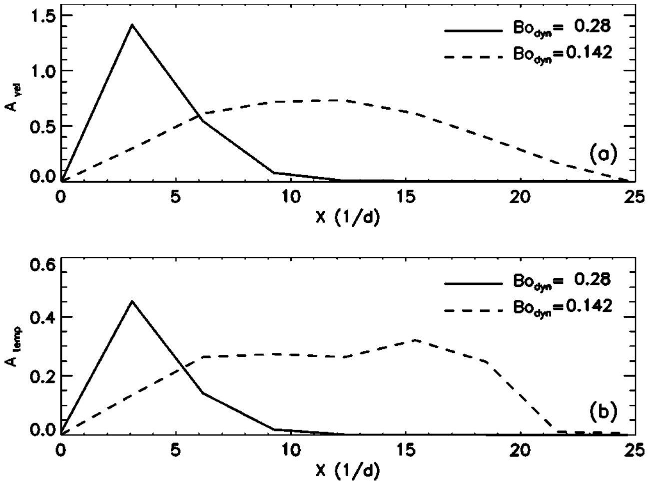

FIG. 10. Results of Fourier spectrum: the distribution of the amplitude of the fundamental frequency of the velocity (a) and temperature (b) along the cavity for different Bond numbers; $\mathrm{Bo}_{dyn}=0.142$, $\mathrm{Ma}=1304$, $f_0=0.519$ and $\mathrm{Bo}_{dyn}=0.28$, $\mathrm{Ma}=989$, $f_0=0.476$.

ence ΔT is lower, so that the steady rolls are not strong enough to cause additional frequencies.

The variation of the amplitude of the Fourier component with the fundamental frequency along the cavity, shown in Fig. 10 for $\mathrm{Bo}_{dyn}=0.142$ and $\mathrm{Bo}_{dyn}=0.28$, confirms the description of the motion given above. The amplitudes are obtained by the Fourier analysis of the time signals $\Theta(t)$ and $V(t)$ recorded at different x positions, and each of them is normalized by the same constant. For $\mathrm{Bo}_{dyn}=0.28$ both amplitudes drastically decrease arriving at the point $x_d=10.6$, and they drop by two orders of magnitude at $x_c=16.7$.

Note that in the case of $\mathrm{Bo}_{dyn}=0.142$, the amplitude of the velocity oscillations, $A_V(x)$ has its maximum in the middle of the cavity and decreases smoothly towards the hot and cold sides, see dashed line Fig. 10(a). The amplitude of the temperature has maximum closer to the hot side, sharply decreasing in the region of the decay of the HTW. Closer to the hot side the amplitude slightly increases again, indicating the oscillations of the stationary roll [see Fig. 10(b) and also Fig. 7]. The different positions of the amplitude maxima of the velocity and temperature indicate the thermal nature of the boundary-generated stationary rolls.

The most amazing case corresponds to $\mathrm{Bo}_{dyn}=0.3$. It is a first sign that the multirolls intend to control the heat and mass transfer in the cavity. For this combination of parameters, the strength of the second roll from the hot side is the same as the strength of the HTW. According to Fig. 11(a), the HTW still exists in small region near the cold wall, $0<x\leqslant 6.8$, followed by the region of decay $6.8<x<9.9$. On the side of the multiroll structure there is also a small region of decay, $14.1<x<15.5$. In the central part, between the regions of the decay of both waves, $9.9<x<14.1$, there is a region of the "shuttle" motions. A roll, pushed by the HTW, moves to the right and after collision with a stationary wave, goes back. The broken lines $x_d=9.9$ and $x_c=14.1$ in Fig. 11 are framed for this region. One may say that the strength of both waves is similar, therefore the motion of the roll(s), confined between them, looks like a motion of a ball pushed from both sides by the elastic walls.

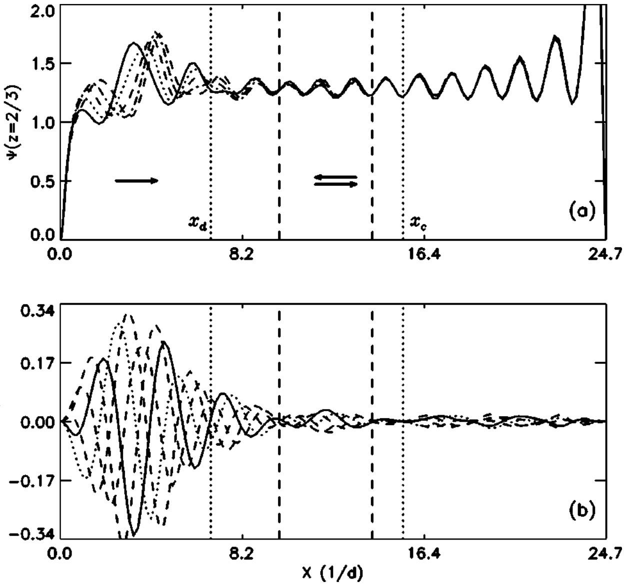

FIG. 11. (a) Instant profiles of $\psi(t_i)$ over the half period and (b) deviation from average over period of oscillations $\tilde{\psi}(t_i)=\psi(t_i)-\psi_{av}$ when $z=2/3$, $\mathrm{Bo}_{dyn}=0.30$, $\mathrm{Ma}=1102$, $\epsilon=0.026$ ($\Delta T=12.2$).

As it is seen from Fig. 11(b), the amplitude of the oscillations in this central area is larger than that in the decay regions. The HTW loses energy in the favor of the stationary wave, and as it follows from Fig. 11, all stationary rolls oscillate with time. The frequency of the oscillations is equal to the frequency of the HTW, but the amplitude of the rolls' oscillations is very small.

Note that the wavelength of a traveling wave in the case $\mathrm{Bo}_{dyn}=0.30$ is significantly larger than that of the steady

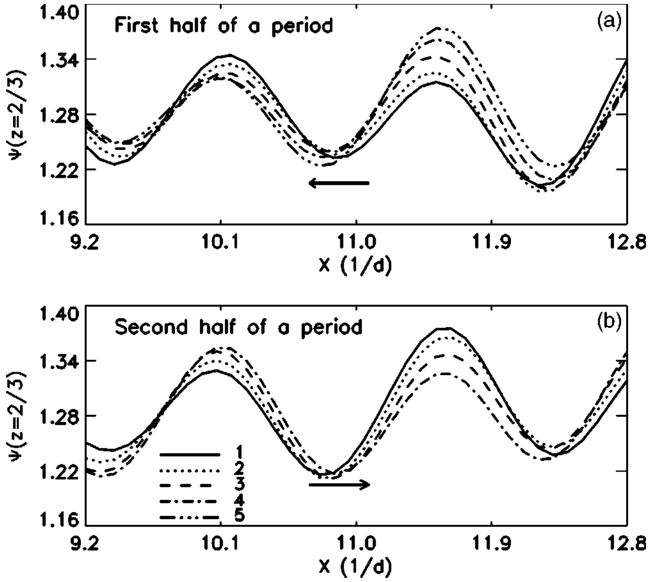

FIG. 12. Instant profiles of $\psi(t_i)$ over (a) the first and (b) the second half of the oscillation period when $\mathrm{Bo}_{dyn}=0.30$. This is the enlarged central part of the Fig. 11(a) clarifying the return motions.

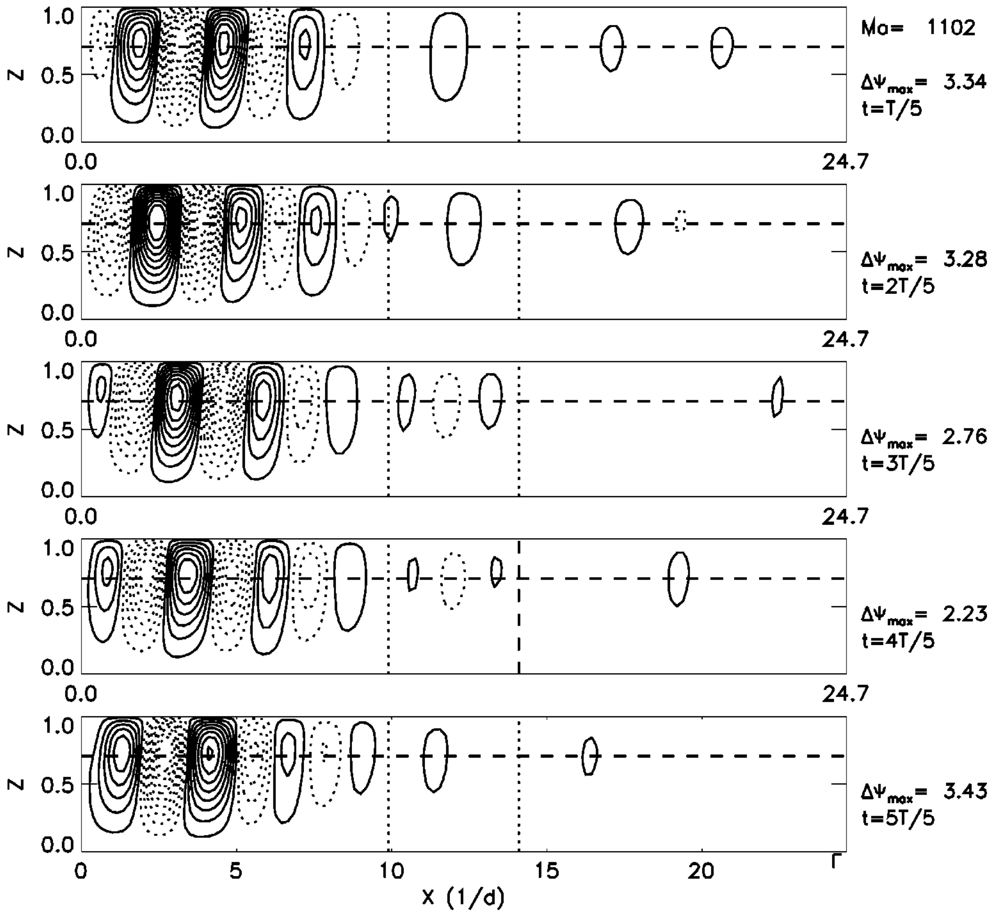

FIG. 13. Snapshots of the deviations of the stream function from average over the period of the oscillations $\tilde{\psi}(t) = \psi(t) - \psi_{av}$ when $\mathrm{Bo}_{dyn} = 0.30$, Ma=1102, $\epsilon = 0.026$. The solid and dashed lines correspond to the negative and positive values of $\tilde{\psi}(t)$.

multicellular structure [see Fig. 11(a)]. The wavelength of the wave propagating on the background of the latter structure is even larger than that of "free" traveling waves [see Fig. 11(b)]. Probably, this circumstance is caused by the difference in the dispersion relation of both kinds of waves (for the same frequency, the wave numbers are different).

The scale of Fig. 11(a) does not allow a clear recognition of the shuttle motions. Therefore the central part of Fig. 11(a) at an enlarged scale is shown in Fig. 12. The instant profiles of $\psi(t)$ are shown separately for the first and the second half of a period, curve 1 corresponds to $t = t_0$, curve 2 corresponds to $t = t_0 + \Delta t$, etc. According to the succession of curves, at the first half of a period the roll moves to the left and at the second half it moves to the right.

The dimensionless wavelength is seen to be a one more proof of the existence of two different mechanisms of the pattern generation on both sides of the cavity. According to the linear theory of Smith and Davis [4] for zero-gravity conditions, the wavelength of the HTW is $\lambda/d \approx 2.4$. Our calculations for the smallest Bond number, $\mathrm{Bo}_{dyn} = 0.08$, give a close value near the cold side, $\lambda/d \approx 2.54$. It is obtained that the wavelength of the HTW practically does not depend upon the Bond number. Even at the transient regime, when $\mathrm{Bo}_{dyn} = 0.28$ and $\mathrm{Bo}_{dyn} = 0.30$, the wavelengths near the cold wall are $\lambda/d = 2.74$ and 2.95, respectively. Note that our results are similar to the experimental results of Ref. [14], where for their highest Bond number, $\mathrm{Bo}_{dyn} = 0.222$, for which they observed the HTW, the measured value of the wavelength was $\lambda/d = 2.70$. Near the hot wall the wavelength is almost twice smaller, $\lambda/d \approx 1.5$, indicating another origin of the flow pattern.

The behavior described above is clearly visible from the snapshots of the function $\tilde{\psi}(x,z,t) = \psi(x,z,t) - \psi_{av}(x,z)$ over the period in the whole cavity in Fig. 13. The isolines of the deviation function $\tilde{\psi}(t)$ are shown inside the whole cavity at five different instants of time during one period of the oscillations. The levels of isolines are equidistant. To present the oscillations with very different amplitudes on both sides, 19 different levels of isolines are plotted. The location of the cells near the cold side at different time moments indicates the propagation of the wave to the right. The presence of some "ghosts" in the right part reveals the oscillations of stationary rolls under the influence of the collision with a HTW.

Let us describe now the evolution of temperature fields. A few, usually ten, snapshots of the temperature have been recorded over period in equidistant time moments $\Delta t = \Pi/N$, here N is the amount of snapshots and Π is a period. The temperature profiles at time instants $\Theta_0(t_i) = \Theta_0(\Delta t i)$ are

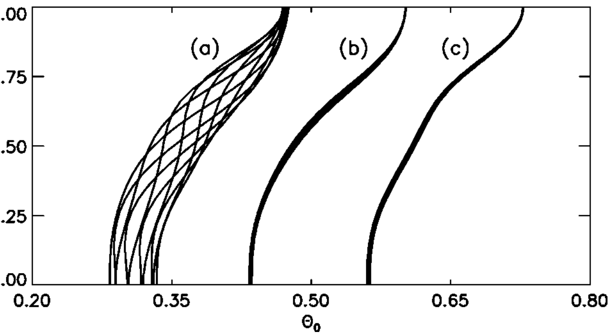

FIG. 14. Snapshots of the temperature $\Theta_0(t_i)$ during one circle of the oscillations for $\mathrm{Bo}_{dyn}=0.3$ at defined horizontal positions; (a) $x=0.25\Gamma$; (b) $x=0.5\Gamma$; (c) $x=0.75\Gamma$ (ten snapshots at each location).

shown in different locations along the cavity in Fig. 14. In agreement with the above described behavior of the flow pattern for $\mathrm{Bo}_{dyn}=0.30$, the largest temperature oscillations are observed in the region controlled by the HTW when $x=0.25\,\Gamma$. The amplitude of oscillations, being smallest on the free surface, is almost constant at the deeper part, $0<z<0.75$. In the region of the shuttle motion, $x=0.5\ \Gamma$, the temperature oscillations are one order of magnitude smaller than at $x=0.25\ \Gamma$, although they are well visible. The maximal variations of the temperature are observed near mid-depth of the cavity, $0.4<z<0.75$. In the region controlled by the steady rolls, $x=0.75\ \Gamma$, the temperature profile is practically unchanged within the oscillation period.

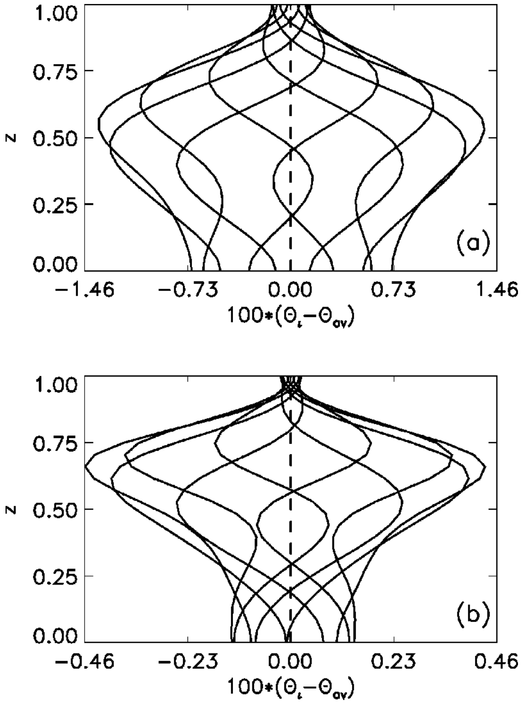

FIG. 15. Deviation of the temperature from the average during one circle of the oscillations at the position $x=\Gamma/2$ (a) $\mathrm{Bo}_{dyn}=0.08$, (b) $\mathrm{Bo}_{dyn}=0.3$.

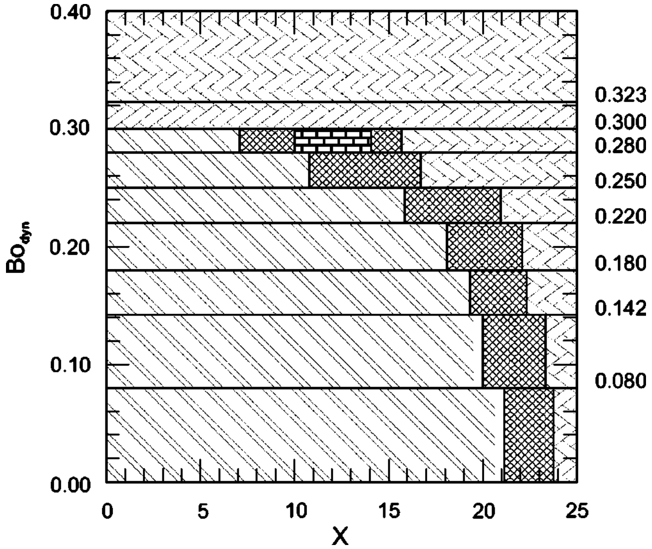

FIG. 16. The coexistence of the different types of motions depending on the dynamic Bond number.

One more confirmation of the fact that we deal with the hydrothermal wave is presented in Fig. 15. In that figure, the deviations of the temperature from the average value during one period of oscillations,

$$\tilde{\Theta}_i=\Theta_0(t_i)-\Theta_{av}, \quad \text{where} \quad \Theta_{av}=\frac{1}{N}\sum_{i=1}^{N}\Theta_0(t_i),$$

are shown. In accordance with the prediction of Smith [6], the maximum amplitude of the temperature oscillations is reached at half a depth. As it follows from Fig. 15(a) for $\mathrm{Bo}_{dyn}=0.08$, when the HTW exists almost in the whole volume, the maximum amplitude is achieved at the depth a little bit higher than $z=d/2$. For the Bond number $\mathrm{Bo}_{dyn}=0.3$, the maximum amplitude is located at $z\approx 0.75d$. Note that this temperature distribution corresponds to the region of the shuttle motion. The minimal amplitude of oscillations in both cases is observed on the free surface.

The coexistence of two different types of motions, the HTW and multirolls structure, and transition between them along the cavity are summarized in the diagram shown in Fig. 16. The values of the Bond numbers, for which calculations have been done, are written on the left side. This diagram is built on the basis of the animation of the numerical results. In the processing of numerical results for the sustained oscillations the short "movies" have been done. It allowed to determine (with some tolerance) regions in space where the HTW collides with the multirolls structure. The various shadings correspond to the different scenarios of the flow organization. Near the cold wall, on the left side, the HTW controls the situation up to $\mathrm{Bo}_{dyn}=0.30$ (shaded by diagonal lines). The region, occupied by the multirolls near the hot wall, is slowly extending coming from the right side, until it conquers the whole cavity, $\mathrm{Bo}_{dyn}>0.3$ (another type of shading). The space, shaded by the mesh, displays either the region where the oscillatory structures, usually the HTW, decay or calm region, e.g., for $\mathrm{Bo}_{dyn}=0.28$. Only for the $\mathrm{Bo}_{dyn}=0.30$ in the central part of the cavity the return mo-

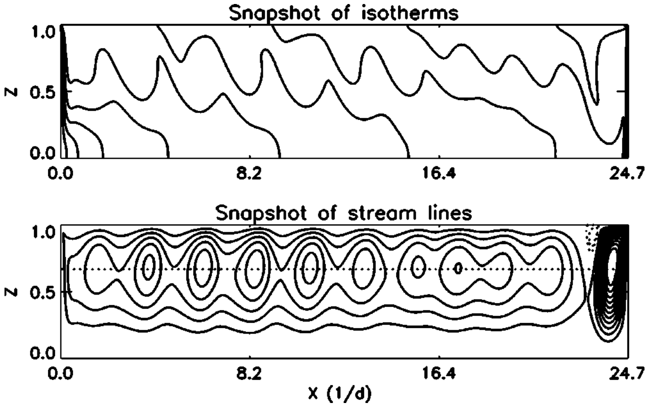

FIG. 17. Snapshot of the oscillatory multicellular state when $\mathrm{Pr}=14.79$, $\mathrm{Bo}_{dyn}=0.728$, $\mathrm{Ma}=1836$, $\epsilon=0.3$ ($\Delta T=13$).

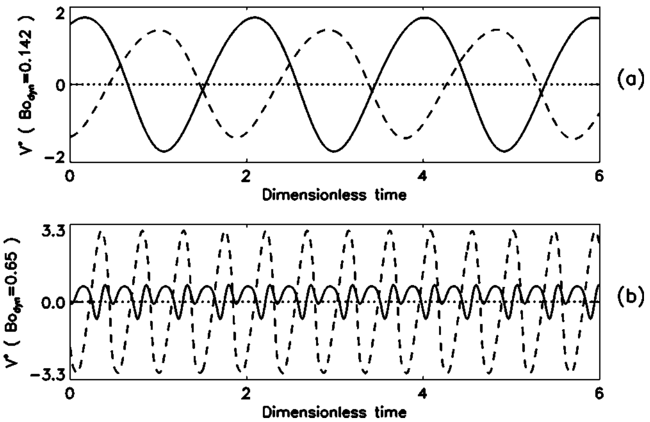

FIG. 18. The dependence of velocity upon time for different regimes of instability, (a) hydrothermal wave, $\mathrm{Bo}_{dyn}=0.142$ and (b) multirolls, $\mathrm{Bo}_{dyn}=0.65$.

tion of a few rolls (kind of "oscillator") has been observed. This is shown by special shading.

E. Multicellular structures and the transition to nonsteady motions for large Bo_{dyn}

For $\mathrm{Bo}_{dyn}>0.3$ the multirolls structure fills the cavity before the instability sets in. For the investigated Bond numbers, 14 corotating rolls are established in the cavity before the onset of the oscillations. The leading role is played by the first roll near the hot side. The observed value of the stream function inside this cell is considerably higher than any other ones throughout the calculations (up to $\epsilon\approx 1$).

Above the threshold of oscillatory instability, just this roll pushes the chain of vortices and the disturbances propagate from the hot to the cold side. The initial impulse is strengthened with the increase of Ma, and eventually at some time instants for certain $\mathrm{Ma}^{*}>\mathrm{Ma}_{cr}$ the small vortex with the opposite direction of the circulation appears near the free surface between the first roll and the second roll. The snapshot of the oscillatory multicellular state in Fig. 17 is chosen in such a way as to demonstrate the existence of this vortex with counter clockwise direction of a circulation. It is shown by the dashed lines in Fig. 17 for the streamlines when $\mathrm{Pr}=14.79$, $\mathrm{Bo}_{dyn}=0.728$, $\mathrm{Ma}=1836$, $\epsilon=0.3$.

It seems that the physical mechanism of instability is similar to those described in Refs. [27,28]. This mechanism is related to the temporal interaction between large-scale thermal structures within the flow field near the hot wall and the temperature sensitive free surface. The transition from steady to oscillatory regime occurs when the fluid motion becomes sufficiently strong, so that the cold tongue (finger), established inside the liquid near the hot wall, is able to influence the thermocapillary surface. On the snapshot of isotherms in Fig. 17, it is clearly seen that the colder region framed by the first isotherm penetrates rather deeply and closely to the hot wall. For supporting oscillations, the area of free surface sensitive to cooling has to lie within the influence of the cold finger.

The first characteristic feature of the side-wall instability is a high temporal frequency. Near the transition between the HTW and multirolls instability ($\mathrm{Bo}_{dyn}=0.3$), the frequency becomes four times larger: the dimensionless frequency for the HTW is practically constant and it is about $f\approx 0.5$, and for the multirolls it begins from $f=2$ and slightly grows with increasing Ma. This is confirmed by Fig. 18, where the dependence of velocity upon time is shown for two different regimes, e.g., $\mathrm{Bo}_{dyn}=0.142$, upper plot, and $\mathrm{Bo}_{dyn}=0.65$, lower plot. The solid curves show normalized velocity $V^{*}(t)=V(t)-0.5(V_{max}+V_{min})$ near the cold side, when $x=3\Gamma/8$ and dashed curves correspond to the velocity near the hot side, when $x=7\Gamma/8$.

For $\mathrm{Bo}_{dyn}\leqslant 0.25$, the velocity and temperature (not shown) oscillations have a perfect sinusoidal form both near the hot and cold walls, only the amplitudes vary. Usually the dependences $\Theta(t)$ and $V(t)$ are out of phase, but the phase shift is constant along the cavity. If we plot the temperature distribution instead of velocity in Fig. 18(a), only the scale would be different. For the transient regime, $0.25\leqslant\mathrm{Bo}_{dyn}\leqslant 0.30$, the time signals look still sinusoidal but their amplitude is differently modulated at the various space points along the cavity (e.g., see Fig. 9).

As soon as the multirolls take power the time signals $V(t)$ and $\Theta(t)$ are not anymore sinusoidal, although periodical and self-sustained.

Just near the hot wall, $x=7\Gamma/8$, the signal $V^{*}(t)$ is quasisinusoidal, but arriving at the center of the cavity the signal already receives a complex shape, although the amplitude is only 2 or 2.5 times smaller. Closer to the cold wall, $x=3\Gamma/8=6.9$, as it shown by solid line in Fig. 18(b), the signal completely changes the shape and the amplitude reduces by approximately ten times. Further the shape of the signal remains approximately the same, but the amplitude continues to decrease, $A_V(x=0.12)=0.1A_V(x=6.9)$. Analyzing the similar signals at other positions along the x axis, one may draw a conclusion that this wave has an amplitude constant in time but varying in space. The qualitative behavior of the temperature is similar, but for the latter regime the phase shift between the temperature and velocity does spatially vary.

To clarify once more the direction of the propagation of the oscillation in the case of high Bond number, the snapshots of the deviations of the stream function from average

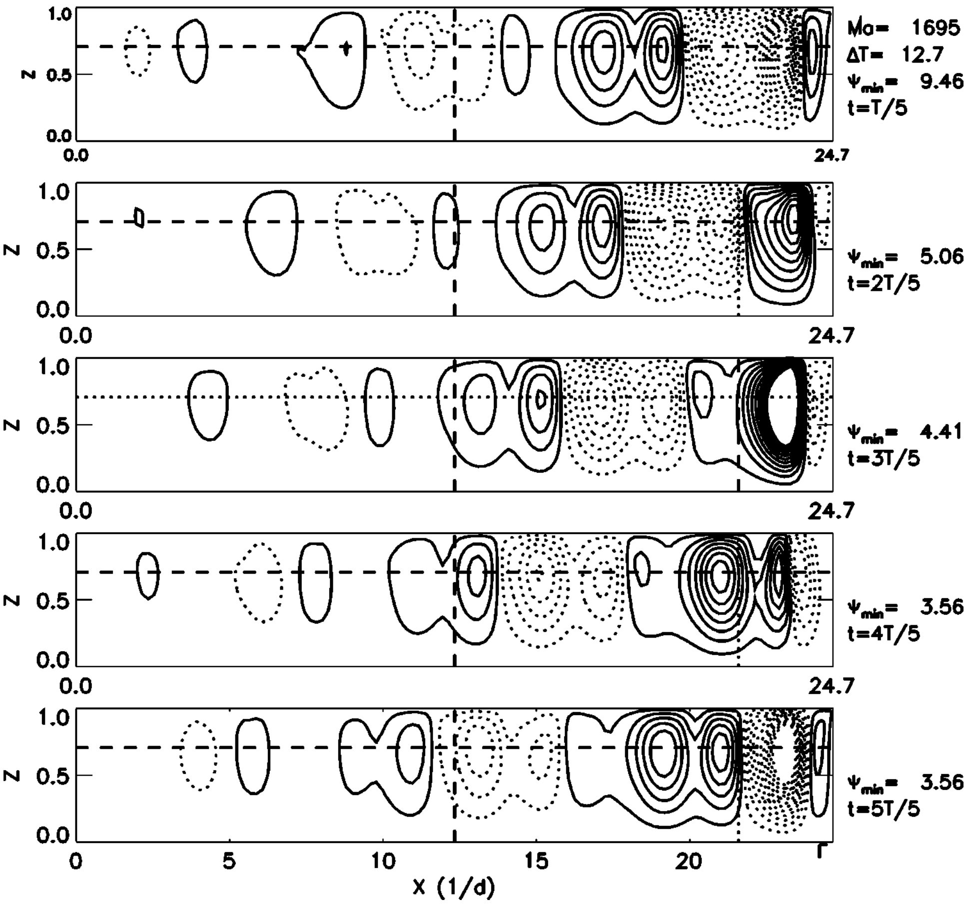

FIG. 19. Snapshots of the deviations of the stream function from average over the period of the oscillations $\tilde{\psi}(t)=\psi(t)-\psi_{av}$ when $\mathrm{Bo}_{dyn}=0.65$, $\mathrm{Ma}=1695$, $\epsilon=0.09$. To show the structure of weak deviations near the cold side $(x=0)$, 21 equidistant isolines are plotted. Moreover, maximal and minimal values of the stream function are reduced by 40%.

$\tilde{\psi}(t)=\psi(t)-\psi_{av}$ over the period of oscillations are shown in Fig. 19 for $\mathrm{Bo}_{dyn}=0.65$, $\mathrm{Ma}=1695$. The amplitudes of oscillations are very different on both sides, therefore the maximal and minimal values of the stream function are reduced by 40% and 21 equidistant isolines are plotted. The levels of isolines are not written in order to simplify the picture.

Intensive oscillations are born at the hot side $(x=\Gamma)$ and then they propagate to the left decaying in space on the background of the system of vortices. The structure starts as a bivortex, but then it loses the bivortical shape due to the decay and smoothening. In the left part of the cavity, the intensity of oscillations is so small that the centers of vortices are motionless. It is worth comparing this picture with a similar one for the small Bond number, see Fig. 13. Comparison clearly demonstrates that for small Bond number deviations spread from the cold to the hot side, while for higher Bond number the oscillations propagate in opposite direction.

The decay of oscillations propagating to the left is compatible with the results of Fourier analysis for $\mathrm{Bo}_{dyn}=0.65$. The results of the temporal Fourier analysis at different points along the cavity are shown in Fig. 20 for the velocity on the free surface. Near the hot side, $x\geqslant 7\Gamma/8$, (first plot) the oscillatory flow practically consists of a single Fourier mode f_0. With receding from the hot wall, at least two higher harmonics $2f_0$ and $3f_0$ with distinguishable amplitude appear in the spectrum. The amplitudes of the main frequency and the first harmonic become equal just after crossing the middle of the cavity. Further to the left, the first harmonic $2f_0$ becomes leading and closer to the cold wall all amplitudes rapidly decrease. Despite the large aspect ratio, the strong interaction of different harmonics is observed. Possibly the amplification of the second harmonics near the cold side is caused by a certain nonlinear interaction between dif-

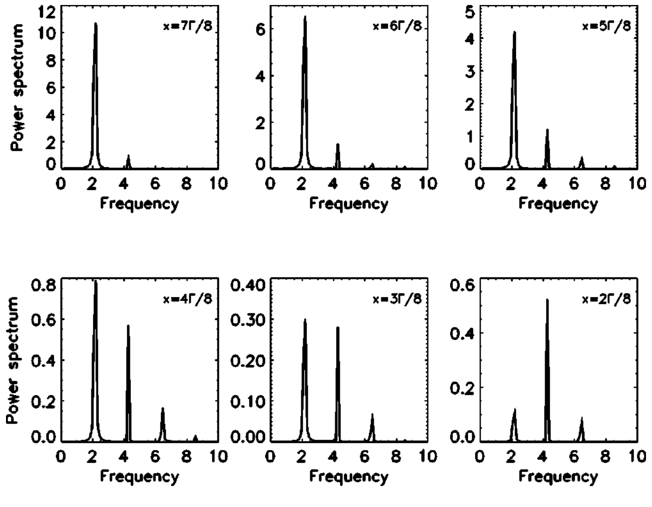

FIG. 20. The temporal power spectrum of the surface velocity at different positions along the cavity when $\mathrm{Bo}_{dyn}=0.65$; $x=0$ corresponds to the cold wall, $x=\Gamma$ corresponds to the hot wall.

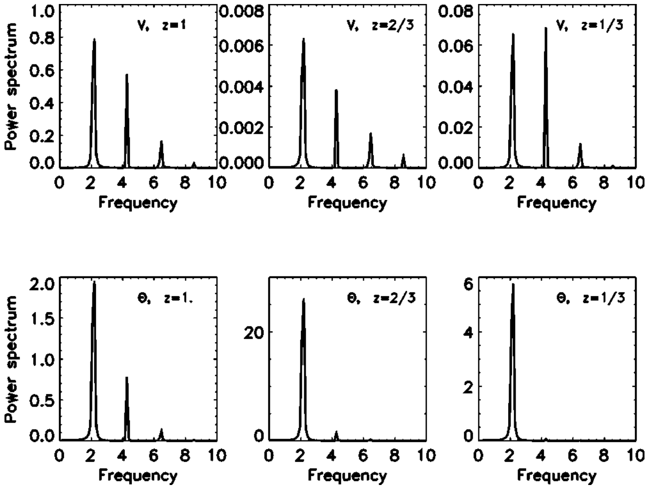

FIG. 21. The temporal power spectrum of the surface velocity and surface temperature at different depths in the center of the cavity; $\mathrm{Bo}_{dyn}=0.65$.

ferent harmonics, which cannot be explained in qualitative terms.

The results of the temporal Fourier analysis at different depths are shown in Fig. 21 for the velocity and the temperature at the middle of the cavity when $\mathrm{Bo}_{dyn}=0.65$. The main frequency of the velocity field and its harmonics have the largest amplitude on the free surface, $z=1$. As the velocity has a minimum at the line $z=2/3$, all amplitudes are smallest at this depth, compare the scales. Closer to the bottom, $z=1/3$, the amplitudes of f_0 and $2f_0$ are equal, although one order of the magnitude smaller than that on a free surface.

The temperature oscillations of the main frequency f_0 retain the leading position in the middle of the cavity for various depths, although the amplitude has a pronounced maximum at the depth $z=2/3$, e.g., $A_\Theta(z=2/3)$ is 28 while $A_\Theta(z=1)=2$.

Above the threshold of instability the amplitude of the spatial oscillations grows with the increase of ϵ. It becomes tight for the 14 rolls to exist together and at certain set of parameters the amount of rolls begin to decrease. The evolution of the number of the rolls versus Marangoni number is shown in Fig. 22 for $\mathrm{Pr}=14.79$. Note that no essential difference in the development of instability was found on comparing the liquids with $\mathrm{Pr}=13.9$ and $\mathrm{Pr}=14.79$, e.g., 1cSt silicone oil and decane.

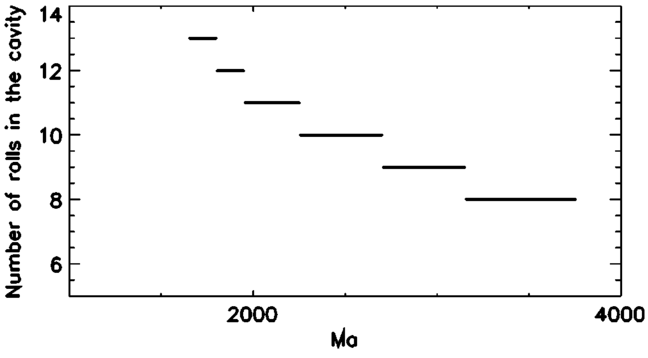

FIG. 22. The amount of rolls in the cavity versus the Marangoni number; $\mathrm{Pr}=14.79$, $\Gamma=24.7$.

V. CONCLUSIONS

Combined thermocapillary-buoyancy convection in shallow cavity with differently heated walls has been investigated numerically. The results are obtained for a fluid of Prandtl number 13.9 with an aspect ratio $\Gamma=24.7$.

The presence of the remote walls drastically changes the flow organization, which would be expected from the results for the infinite layer: (a) quantitatively—due to the temperature drops near the rigid walls and (b) qualitatively—due to the appearance of a new type of instability.

In the previous sections, we have shown that there exist two various types of instabilities which are determined by two control parameters: the dynamic Bond number and Marangoni number. For relatively small Ma and Bo_{dyn} numbers the steady convective cell appears in the volume, which is split into a stronger cell near the hot wall and a larger but weaker cell in the rest of the cavity.

With increasing Marangoni number this steady (bicellular or multicellular) flow gives rise to the oscillatory flow (hydrothermal wave). With increasing dynamic Bond number, the small cell near the hot side grows and other cells appear which spread towards the cold wall. The intensity of the motion in the corotating cells rapidly diminishes with the distance from the hot end. The multirolls invade the cavity before the oscillatory instability sets in. The transition from a steady bicellular flow to a steady multicellular flow is not a result of instability.

The results of calculations are summarized as a stability diagram $\mathrm{Ma}_{cr}(\mathrm{Bo}_{dyn})$ in Fig. 4. The different types of instability have been identified unambiguously: for the small Bond numbers, $\mathrm{Bo}_{dyn}<0.3$, the instability begins as a hydrothermal wave which is generated on the cold wall. This hydrothermal wave, moving from the cold side, appears earlier than the rolls coming from the hot side conquering the whole cavity.

Contrary to the majority of the experimental results in the extended layers, a genuine unicellular flow was never observed at the threshold of the appearance of the HTW. For the smallest values of the dynamical Bond number Bo_{dyn}, a bicellular flow was established in the cavity. For larger values of Bo_{dyn}, several cells were developed near the hot wall. Probably, a special experimental technique should be applied in order to explore the separation of the vortices at small ΔT near the hot wall. Thus, the term unicellular flow is not sufficiently accurate for the description of the flow prior to the onset of the HTW.

For the larger Bond numbers, $\mathrm{Bo}_{dyn}\geqslant 0.323$, the threshold of the instability represents the transition from steady multicellular flow to oscillatory multicellular flow. Contrary to the HTW, in the latter regime the disturbance wave is generated at the hot wall and propagates to the left.

The oscillation frequency of the multicellular flow is about four times higher than the frequency of the HTW.

For the intermediate interval of Bo_{dyn} the parallel flow is unstable with respect to HTW, but the multicellular periodic structure generated by the side-wall perturbation is stable. The simulations revealed some nontrivial features of the interaction between the instability-generated HTW and wall-generated steady patterns. A HTW typically decays in the region of steady pattern. However, it induces oscillations of the wall-generated system of vortices. The HTW penetrating into the region occupied by the steady pattern keeps its frequency but changes its wavelength. Under the conditions of a coexistence of both types of motion, the HTW near the cold wall and oscillating multicellular structure near the hot wall, satellite frequencies of the oscillations appear, which lead to a more complicated, quasiperiodic, temporal behavior of waves.

The results of the simulations concerning the instability threshold coincide qualitatively with the prediction of the linear theory [16] that takes into account the difference between the convective and absolute instabilities, as well as the penetration of side-wall disturbances into the cavity.

The comparison between the results of simulations and the experimental data [14,15] is presented in Fig. 4. For the values of the Bond number, when the flow is controlled by the instability-generated HTW, the results for the instability threshold and the frequency of the oscillations are in a good agreement.

For the oscillatory multicellular flow, the available experimental and numerical results correspond to the different sets of parameters. To the best of our knowledge, there are no experimental results in the transient regime.

The validation of the predictions of the nonlinear simulations can be done by means of new experiments.

ACKNOWLEDGMENTS

A.A.N. acknowledges the hospitality of the Microgravity Research Center at Free University of Brussels. The collaborative work was supported in part by the EU network ICOPAC.

[1] H. C. Kuhlmann, *Thermocapillary Convection in Models of Crystal Growth* (Springer-Verlag, Berlin, 1999).
[2] R.V. Birikh, J. Appl. Mech. Tech. Phys. **7**, 43 (1966).
[3] M.V. Volkoviski, C. R. Acad. Sci. **200**, 1285 (1935).
[4] M.K. Smith and S.H. Davis, J. Fluid Mech. **132**, 119 (1983).
[5] M.K. Smith and S.H. Davis, J. Fluid Mech. **132**, 145 (1983).
[6] M.K. Smith, Phys. Fluids **29**, 3182 (1986).
[7] S.H. Davis, Annu. Rev. Fluid Mech. **19**, 403 (1987).
[8] J. Xu and A. Zebib, J. Fluid Mech. **364**, 187 (1998).
[9] P.M. Parmentier, V.C. Regnier, and G. Lebon, Int. J. Heat Mass Transfer **36**, 2417 (1993).
[10] A.B. Ezersky, A. Garcimartin, H.L. Mancini, and C. Pérez-Garcia, Phys. Rev. E **48**, 4414 (1993).
[11] J.F. Mercier and C. Normand, Phys. Fluids **8**, 1433 (1996).
[12] D. Schwabe, U. Möller, J. Schneider, and A. Scharmann, Phys. Fluids A **4**, 2368 (1992).
[13] C. De Saedeleer, A. Garcimartin, G. Chapeveyer, and J.K. Platten, Phys. Fluids **8**, 670 (1996).
[14] R.J. Riley and G.P. Neitzel, J. Fluid Mech. **359**, 143 (1998).
[15] J. Burguete, N. Mukolobwiez, F. Daviaud, N. Garnier, and A. Chiffaudel, Phys. Fluids **13**, 2773 (2001).
[16] J. Priede and G. Gerbeth, Phys. Rev. E **56**, 4187 (1997).
[17] E. M. Lifshitz and L. P. Pitaevskii, *Physical Kinetics* (Pergamon Press, Oxford, 1981).
[18] S.P. Kuznetsov, E. Mosekilde, G. Dewel, and P. Borckmans, J. Chem. Phys. **106**, 7609 (1997).
[19] P. Andresén, M. Bache, E. Mosekilde, G. Dewel, and P. Borckmans, Phys. Rev. E **60**, 297 (1999).
[20] O.A. Nekhamkina, A.A. Nepomnyashchy, B.Y. Rubinstein, and M. Sheintuch, Phys. Rev. E **61**, 2436 (2000).
[21] V.M. Shevtsova, D.E. Melnikov, and J.C. Legros, Phys. Fluids **13**, 2851 (2001).
[22] A. Samarskii, *Introduction to the Numerical Methods* (Nauka, Moscow, 1983) (in Russian).
[23] A. Zebib, G.M. Homsy, and E. Meiburg, Phys. Fluids **28**, 3467 (1985).
[24] M. Ohnishi, S. Yoshihara, and H. Azuma, Acta Astron. **26**, 685 (1992).
[25] G. De Vahl Davis, Int. J. Numer. Methods Fluids **3**, 249 (1983).
[26] V.M. Shevtsova and J.C. Legros, Acta Astron. **52**, 541 (2003).
[27] L.J. Peltier and S. Biringen, J. Fluid Mech. **257**, 339 (1993).
[28] V.M. Shevtsova and J.C. Legros, Phys. Fluids **10**, 1621 (1998).